JASA ARTICLE

Signal-to-noise ratio of diverging waves in multiscattering media: Effects of signal duration and divergence angle

Yasin Kumru[a] and Hayrettin Köymen[b]
Electrical and Electronics Engineering Department, Bilkent University, Ankara, 06800, Turkey

ABSTRACT:
In this paper, SNR maximization in coded diverging waves is studied, and experimental verification of the results is presented. Complementary Golay sequences and binary phase shift keying modulation are used to code the transmitted signal. The SNR in speckle and pin targets is maximized with respect to chip signal length. The maximum SNR is obtained in diverging wave transmission when the chip signal is as short a duration as the array permits. We determined the optimum diverging wave profile to confine the transmitted ultrasound energy in the imaging sector. The optimized profile also contributes to the SNR maximization. The SNR performances of the optimized coded diverging wave and conventional single-focused phased array imaging are compared on a single frame basis. The SNR of the optimized coded diverging wave is higher than that of the conventional single-focused phased array imaging at all depths and regions.
https://doi.org/10.1121/10.0009410

(Received 4 August 2021; revised 14 January 2022; accepted 18 January 2022; published online 10 February 2022)

[Editor: Libertario Demi] Pages: 955–966

I. INTRODUCTION

The conventional ultrasound imaging techniques using phased arrays employ focused beam transmissions for every image line.[1] The transmitted signals are superimposed constructively in the focal region, and, hence, the signal-to-noise ratio (SNR) improves in the focal region as the transmitted signal duration increases. However, the transmitted signals are spread over a broader region in diverging wave imaging (DWI) and add up destructively in the field due to the unmatched phases.[2–9] This effect imposes a limitation for SNR and penetration depth in DWI.[1] The effect is further aggravated when the DWs propagate in a multiple-scattering and diffracting medium since the medium also causes the ultrasound beam to diverge and produces interference in the sound field.[10–12] Furthermore, when the beam width in DWI is determined using only geometric considerations, a significantly larger insonified sector emerges due to multiple scattering and diffraction, which causes a waste of available energy.

In this respect, we investigated the effect of the chip signal duration on SNR experimentally in a multiple-scattering and diffracting medium. We obtained the maximum SNR at the longer distance when the chip signal duration is short enough to correspond to the transducer bandwidth. SNR deteriorates when the signal duration increases. We also determine the required beam width in coded DWI, which adequately confines the ultrasound beam energy into the sector to be imaged and contributes to SNR maximization. We compared the SNR of optimized coded DWI to that of the conventional single-focused phased array imaging (CSFI).[13,14]

The use of several steered DWs with the coherent spatial compounding technique increases the SNR and penetration depth.[15–17] However, this method is susceptible to motion artifacts, and the number of the compounded waves must be limited.[17] The motion compensation integrated with the compounding technique further improves the SNR and penetration depth.[18]

Coded excitation also increases the SNR and penetration depth. Takeuchi[19] uses the coded excitation for medical ultrasound imaging. Encoding with chirp signals,[20–23] Barker codes,[24] m-sequences,[25,26] and complementary Golay sequences (CGSs),[27,28] have been studied. Some researchers used both chirp signals and CGSs to make a performance comparison.[29–34] Only CGSs provide range lobe cancellation among all coding sequences. However, they require two successive transmissions and reduce the frame rate to half.[33] Using CGSs and orthogonal CGSs with DW transmission enables SNR improvement compared to uncoded DW transmission.[35–37] The studies on coded excitation employ different chip lengths such as half,[34] one,[24,28,34,36] one and a half,[35,37] two,[27,30–33] and five-cycle/chip.[29] The other studies[25,26] reviewed in this work have no relevant data on chip length.

In addition to the coding sequences, another approach to obtain coding is to use matrix-based coding techniques. Hadamard coding,[38,39] its extended versions,[40–42] and S-sequence coding[43] techniques benefit from the matrix-based coding. The experimental results show that encoding with matrices also improves the SNR and penetration depth.

The attenuation in the tissue impairs the performance of coded signals in medical ultrasonic imaging. The correlation between the received signal and the reference signal deteriorates at the deeper imaging regions. The attenuation

[a]Electronic mail: yasin.kumru@bilkent.edu.tr
[b]ORCID: 0000-0002-9768-2110.

compensation with various compression filters[44] or a frequency downshift estimator[45] for coded transmission offers SNR improvement.

The layout of this paper is as follows: In Sec. II, we present the methods used in this study. Section III describes the construction of the reference signal used in the receiver and the compensation of the reference signal for the frequency-dependent attenuation. Section IV gives the optimization of the DW profile for a given field of view. We experimentally evaluate the effect of chip signal length on SNR in Sec. V. We compare the performances of the optimized coded DWI and CSFI in terms of SNR and signal-to-speckle ratio (SSR) in Sec. VI. In Sec. VII, we discuss the limitations and potential improvements of SNR maximization in coded DWI.

II. METHOD

We used coded DWI in this study. We coded the transmitted signals using 8-chip length CGSs with 0.5, 1, 1.5, and 2 cycle/chip to investigate the chip length effect on the SNR. The CGSs used for coding are discussed in Sec. II A. The receiver for coded signals incorporates a matched filter (MF) at reception. MF is implemented as a correlation receiver, the structure of which is presented in Sec. II B.

We compared the SNR performance of a single DWI frame to CSFI using the same chip signal duration. The CSFI provides the constructive addition of the pressure signals in the focal zone and yields high resolution and maximum achievable SNR in the region. Therefore, we used the focal zone of CSFI as a reference for SNR comparison. We used 181 steered and focused beam transmissions to construct the image scan lines. The steering angle ranged from $-45°$ to $45°$, and was spaced at $0.5°$ intervals. We focused each transmission at a 40 mm distance from the transducer array center. All array elements were used in each transmit and receive event. We applied receive beamforming, a delay-and-sum beamformer, directly on the raw data at each array element to form a scan line along the beam axis.

A Gaussian filter (GF) centered around 7.5 MHz was applied to the beamformed signal to reduce the out-of-band noise and interference components before envelope detection. The transfer function of the GF is given by[46]

$$H_{GF}(\omega) = \frac{\sqrt{2\pi}}{\sigma_\omega} e^{-j\omega/c_0} e^{-(\omega-\omega_c)^2/2\sigma_\omega{}^2}, \tag{1}$$

where c_0 is 1450 m/s, ω_c is the center angular frequency, and $\sigma_\omega/(0.425\ \omega_c)$ is the –6 dB fractional bandwidth of the GF. The fractional bandwidth is 63% when σ_ω is 1.25×10^7. We then applied envelope detection.[46] We referred to this technique as CSFI-GF.

Applying matched filtering to CSFI is expected to increase the SNR further in the focal region. Therefore, we also implemented CSFI with MF to compare with coded DWI, although this method is not employed in practice. We referred to this scheme as CSFI-MF in this study. The MF implementation in CSFI is exactly similar to the implementation used in coded DWI.

We did not employ transmit and receive apodization in this study.

A. Coded transmission

The use of coded signals increases the available energy at a given peak transmitted pressure without sacrificing bandwidth.[31] This property improves the SNR and related performance in ultrasound imaging. We used coded transmission in this work because it enables sufficiently large penetration depth so that the SNR dependence to chip signal length is clearly observable.

The coded transmission correlation coefficient is at a maximum only when the coefficient phases match.[47] The lower correlation levels are referred to as code range lobes. The CGSs have a unique property in that they offer a zero-code range lobe. A CGS consists of a pair of sequences, CGS(A) and CGS(B). The sum of the autocorrelation functions of two sequences doubles at zero phase shift, at other phase shifts this sum is zero.[48] We used the regular implementation of the coded signals and binary phase shift keying (BPSK) for modulation, where the bit value of "+1" corresponds to the 0° chip signal phase, and "−1" corresponds to the 180° phase. In coded signals, the symbol used for each code bit is referred to as a chip (e.g., the length of an 8-bit coded signal is 8-chip long). Table I shows the bipolar representation of the CGSs used in this study.

B. Receiver structure

The MF properties are determined by the properties of the coded transmit signal, which is modified by the transducer and medium attenuation. We employed the correlation receiver implementation, which is common in real-time applications.[49]

Figure 1 shows the transmitter and receiver configuration used in this work for CGS-coded DW excitation. Time delays are applied to each array element to achieve the required wave profile. First, we transmit CGS(A) coded signals from the transducer array. The same array receives the reflected waves. We filtered the received signals at each array element using the MF consisting of a mixer and integrator.

The MF output for the ith array element $\hat{R}_{ys,i}$ is expressed as

TABLE I. Bipolar representation of the 8-chip CGSs used in DWI. BPSK is used for modulation. The bit value "+1" corresponds to the 0° chip signal phase, and "−1" corresponds to the 180° chip signal phase. 180° phase transition occurs in the coded signals when the bit in the sequence changes from "+1" to "−1" or vice versa.

Code length	Sequence type	Bipolar representation
8	CGS(A)	{+1 +1 − 1 −1 − 1 +1 − 1 +1}
8	CGS(B)	{+1 +1 +1 +1 − 1 +1 +1 − 1}

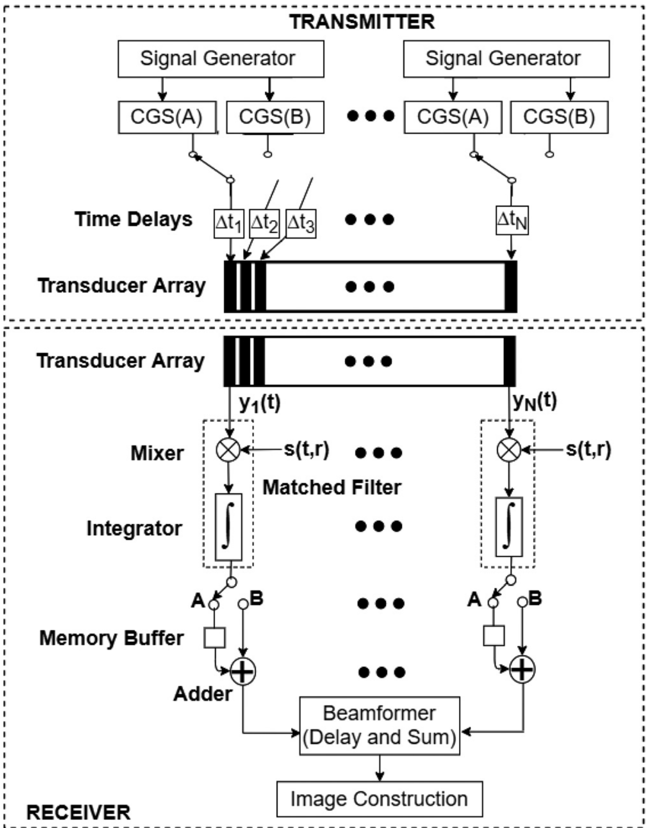

FIG. 1. Transmitter and receiver configuration for coded excitation in DWI. CGS(A) is a Golay sequence, and CGS(B) is its complementary sequence. The transducer elements are driven by CGS(A) and CGS(B) coded signals successively with appropriate time delays to form a diverging wavefront. The same transducer is used for both transmission and reception. A matched filtering is applied to received data. The resulting MF output is beamformed and post-processed to construct the ultrasound image.

$$\hat{R}_{ys,i}(m) = \sum_{k=0}^{K-1} y_i(m+k)s_r(k), \tag{2}$$

where $y_i(l)$ is the lth sample of the received signal at the ith array element, and $s_r(k)$ is the kth sample of the reference signal with length K. For example, K is 146 for the 8-chip coded signal with 1-cycle/chip and 218 for 2-cycle/chip. Note that the increase in reference signal length is less than two folds due to the presence of the transducer transient response in each chip.[50] We compensated the reference signal for the attenuation in the medium, and it was updated 12 times at every 0.5 cm depth. The depth index, r, refers to the updated reference signal, where r ranges from 1 to 12. We describe the attenuation compensation method in Sec. III. The MF output for CGS(A) coded transmission is buffered until the CGS(B) coded transmission data is collected. Then, we added the MF outputs at each array element for two transmissions. The resulting signals are then beamformed using a delay-and-sum receive beamformer[46] to form the image scan lines. We employed Hilbert transform-based envelope detection,[46,51] on the scan line data to obtain envelope information, which was subsequently used for SNR calculation.

C. Measurement setup

We collected the data using the ultrasound research scanner; Digital Phased Array System (DiPhAS, Fraunhofer IBMT, Frankfurt, Germany). The receive record length is 95 μs, and the sampling rate is 80 MHz. We used a phased array transducer (Fraunhofer IBMT, Frankfurt, Germany) operating at 7.5 MHz center frequency with a nominal fractional bandwidth of 70%. There are 128 elements in the array, and the element pitch is 0.1 mm. The transmitted signals are pulse width modulated (PWM) signals.[50] The driving signal amplitude is kept constant at 70 V, which yielded 140 V peak-to-peak amplitude. The fractional bandwidth of the two-way transfer function of the transducer is 67%.

We used a phantom constructed of rubber-based tissue-mimicking material (model 550, Breast & Small Parts Phantom, ATS Laboratories, Bridgeport, CT) for the measurements. Figure 2 shows the phantom structure consisting of monofilament nylon line targets (pin targets) and tissue-mimicking cylindrical targets of varying sizes and contrasts. The pin targets have a diameter of 50 μm. The attenuation in the phantom is 0.5 dB/cm/MHz, and the sound velocity is 1450 m/s at 23 °C. We recorded the phantom temperature and the ambient temperature during the measurements.

D. Signal energy

The amplitude unit in this study is the least significant bit (LSB) of the analog to digital converter in DiPhAS. We refer to the squared instantaneous amplitude (LSB^2) as the instantaneous signal power in this work. The signal energy over a certain period is proportional to the sum of the squares of instantaneous amplitude over that period multiplied by the receiver sampling interval, Δt, as given in Eq. (3). It has units of LSB^2-s. Δt is 12.5 ns in this study,

$$E_i = \Delta t \sum_{q=1}^{Q} y_i^2(q). \tag{3}$$

E. SNR measurement

Though generically, SNR is defined as the ratio of the signal power to noise power and expressed in dB,[52] in

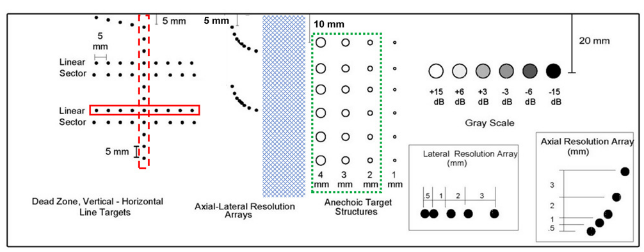

FIG. 2. (Color online) The structure of the commercial ultrasound phantom used in the measurements. The rubber-based tissue-mimicking material has an attenuation of 0.5 dB/cm/MHz and a sound speed of 1450 m/s at room temperature. The solid and dashed rectangles indicate the horizontal pin targets at 40 mm depth and the vertical pin targets, respectively. The cross-hatched rectangle indicates the speckle region. The dotted rectangle indicates the anechoic cysts with 4 mm, 3 mm, and 2 mm diameter.

medical ultrasound imaging, SNR is regarded as speckle to noise ratio and measured as SNR_{+1}, as given in Eq. (4).[53] Since the received signal already contains noise,

$$SNR_{+1} = 10\log_{10}\left(\frac{P_{speckle}}{P_{noise}} + 1\right), \tag{4}$$

where $P_{speckle}$ is the speckle power, and P_{noise} is the noise power. SNR_{+1} is similar to SNR for large values. The speckle power is equal to noise power when SNR_{+1} is 3 dB. Penetration depth is the depth at which SNR_{+1} falls below 6 dB (Ref. 53) and can be determined from SNR measurements.

1. Noise level estimation using noise measurements

We recorded the received noise in each channel without any transmission. The array was kept acoustically in contact with the phantom surface to ensure the noise contribution of the radiation resistance. We processed each channel noise exactly similar to the way the received signal is processed in the respective imaging technique. We calculated the noise power at every delay (depth) as the average of the squared noise signal amplitude (in units of LSB^2) of independently taken 13 noise measurements.

The noise analysis in this study illustrates the correct contribution of radiation resistance noise (which has a colored spectrum), noise due to transducer losses, and preamplifier noise. The total of the transducer originated noise and electronic noise power at each channel and at all delays must be accurately measured to assess the SNR reliably. This is ensured by using adequate fixed gain at the preamplifier stage in both noise and signal measurements to keep the total noise level well above the quantization noise. Therefore, we applied a 22 dB (of 45 dB, the total dynamic range for programmable gain in DiPhAS) fixed gain to ensure an accurate noise contribution in every channel at all delays in all measurements. We limited the time-varying gain to 2.3 dB/cm to avoid any accidental signal saturation. Any further gain can be applied in post-processing without affecting the SNR since all the noise in the received signal is recorded with high fidelity.

2. Speckle signal level estimation using speckle measurements

The speckle signal is the consequence of ultrasonic waves traveling in inhomogeneous media.[12] The signal temporal variation has a random nature due to the random distribution of the inhomogeneities and the multiple-scattering structure of the media. The variance of the signal amplitude can be quite large but smoothing the speckle signal is possible by averaging statistically independent signals. The signal temporal variation changes if either the signal spectrum changes or the transducer spatial position is changed. The frequency spectrum is determined by the signal properties, particularly the duration, which is an optimization parameter in this work.

We made 11 transmissions at different transducer positions for each chip length to have statistically independent speckle data. We moved the transducer array across the phantom surface at approximately 1 mm steps. The speckle region (no targets) is cross-hatched in Fig. 2. We calculated the average speckle signal amplitude as follows: We first calculated the speckle power (in LSB^2) at every delay as the square of the amplitudes in each recording. Then, we calculated the average power of 11 recordings. Finally, we calculated the average speckle amplitude as the square root of the average power.

III. REFERENCE SIGNAL IN ATTENUATING MEDIUM

The correlation receiver requires a reference signal to compress the received signal. SNR is maximized if the received data contains the replicas of the reference signal.[54] The transducer transfer function modifies the driving transmit waveform significantly. Furthermore, the pressure waveform changes as the wave travels through the medium. The energy in the higher frequency range is absorbed more, and the signal mean frequency decreases with depth. Therefore, the reference signal must be modified to match the received pressure from different depths for higher correlation. We compensated the two-way transmitted-and-received signal for the nominal frequency-dependent attenuation. We used the resulting signal as the reference signal in the correlation receiver. We showed that using the compensated signal as the reference signal improves the SNR at the correlator output by up to 6 dB compared to an uncompensated signal. Using the driving transmit waveform as a reference signal causes SNR degradation, since the driving transmit waveform differs significantly from the received echoes.

We used two reference signals in DWI, one for each CGS. The reference signal must be a two-way transmitted-and-received signal to include the effect of the transducer transfer function. We measured the two-way transmitted-and-received signal in freshwater. A highly reflective material, a thick iron plate, was immersed in the water at a depth of 5 cm (approximately). We transmitted from the mid-element, the 64th element, of the phased array transducer and conducted pulse-echo measurements for all chip lengths. The attenuation in freshwater is negligible compared to tissue attenuation. These signals approximate the unattenuated reference signals for each array element since the two-way electro-mechanical transfer functions of all combinations of the transducer elements are not exactly the same.

The attenuation prevents the perfect cancellation of code range lobes of the Golay pairs.[31] This attenuation effect must also be imposed on the reference signal to improve the MF output in the attenuating medium. We applied attenuation compensation to the two-way transmitted-and-received signal at every 0.5 cm up to 6 cm depth. We performed this compensation on the reference signal in the frequency domain by applying exponential attenuation at the aforementioned depths. We first transformed the uncompensated reference signal, $s(t)$, into the frequency domain and obtained $S(f)$. We performed the attenuation compensation on $S(f)$ as

$$S_r(f) = S(f)\, e^{-\alpha f(2r)} \tag{5}$$

to obtain the compensated reference signal $S_r(f)$ transform for depth r in cm, where f is the frequency in MHz and α is the nominal attenuation coefficient of the phantom, which is 0.057 Nepers/cm/MHz. We then transformed $S_r(f)$ back to the time domain and obtained $s_r(t)$.

After applying attenuation correction, we normalized the energy of each signal. The energy of each signal is 8 LSB^2-s for all coded signals, regardless of their duration. We used these fixed-energy reference signals in the MF. When a fixed energy reference signal is used in the correlator, the gain in the correlator remains the same for all reference signals. Figure 3 shows the 8-chip CGS(A) coded reference signals with 0.5, 1, 1.5, and 2 cycle/chip. The amplitude of the reference signals with longer chips is lower in fixed energy reference signals. The bit and phase transitions are delineated in Fig. 3(d). Note that 180° phase transitions are clearly visible at 0.5 cm and 1.5 cm depths when the coded signal bits go from "+1" to "−1" or vice versa. The phase transition instants are also visible. Attenuation compensation distorts the reference signal. The phase transitions become visually less observable at longer ranges, 2.5 cm and 4.5 cm depths. Similar behavior is also visible in Figs. 3(a)–3(c).

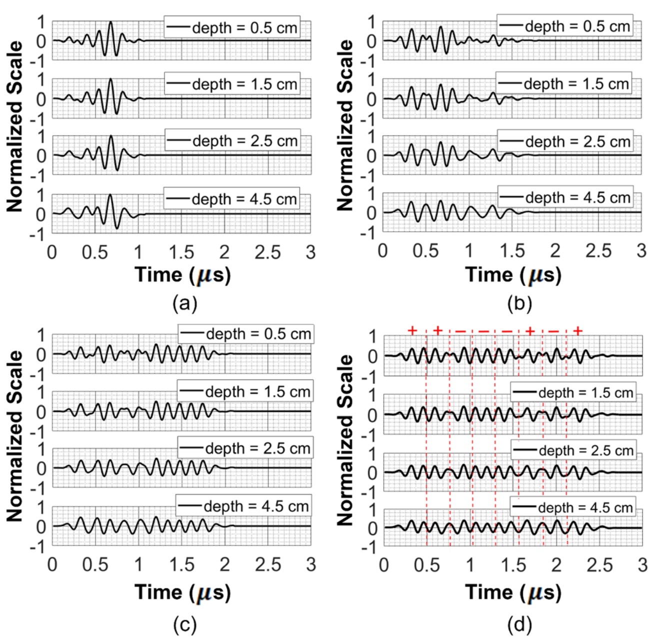

FIG. 3. (Color online) Received signals on the 64th element of the phased array transducer after attenuation compensation. All signal energy is fixed at 8 LSB^2-s. 8-chip CGS(A) coded received signal with (a) 0.5-cycle/chip, (b) 1-cycle/chip, (c) 1.5-cycle/chip, (d) 2-cycle/chip. The bit transitions and phase transition instants are marked for convenience. Every row within each figure corresponds to adaptive attenuation compensation with respect to depths of 0.5, 1.5, 2.5, and 4.5 cm (return path length of 1, 3, 5, and 9 cm), respectively.

On the other hand, since the reference signal used in the MF of CSFI-MF is only a 1-cycle signal, i.e., 1 chip of 1-cycle/chip, its energy is 1 LSB^2-s.

IV. CONFINING THE ENERGY INTO THE REGION OF INTEREST

Keeping the transmitted ultrasound energy within the region of interest is crucial for SNR improvement in DWI. We determine an optimum DW profile to adequately confine the transmitted energy into the sector to be imaged. Using this profile yields the required beam width and contributes to the SNR improvement.

A. Geometry for DW transmission

We obtained the DW profile by applying appropriate phases to array elements so that a cylindrically DW emanates from the array. We determined the phase profile used for a particular DW by the geometry given in Fig. 4, where the transmitted wave is assumed to be generated by an equivalent virtual source.[16] The assumed virtual source is a cylindrical omnidirectional line source positioned behind the transducer array center at a distance of r_v. The omnidirectional cylindrical wave is assumed to be windowed by the array aperture; thus, the insonification sector is established. The element pitch, d, is half of the wavelength at 7.5 MHz. The aperture length is Nd, where N is 128. When the delay profile is configured for a short r_v, the virtual source is close to the aperture, and the total available energy

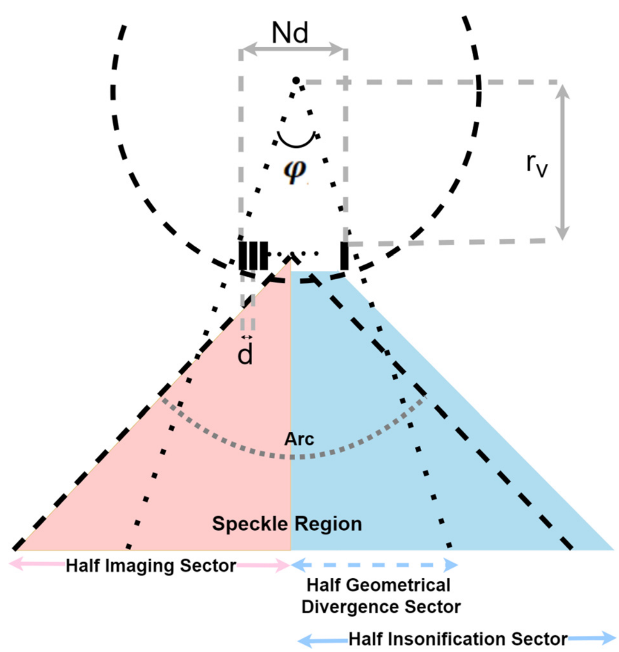

FIG. 4. (Color online) The geometry used to derive a phase profile for a particular DW. For a given aperture, the virtual source distance, r_v determines the geometrical divergence sector. φ is the geometrical divergence sector angle. The time delays applied to each array element is calculated for the geometrical beam width of φ. Insonification sector is wider than the geometrical divergence sector due to the diffraction. The arc in speckle region is also shown along which SNR is measured to determine the appropriate virtual source distance, and thus, the required beam width.

diverges to a wide insonification sector. When the profile is set for a long r_v, energy is confined to an acute sector. Actual energy distribution in the sector differs from the geometrical predictions due to diffraction and multiple scattering.

Maximum SNR at the central region is obtained when r_v is as large as possible, yet r_v must be low enough to adequately insonify the imaging sector, which is 90° in this study. We adopted a criterium based on the SNR for adequate insonification within the imaging sector. We determined the r_v such that the SNR difference between the center and the outermost regions in the imaging sector is 3 dB. We measured the SNR of the coded DWI in the speckle region along arcs for different virtual source positions. An arc, shown in Fig. 4, constitutes equidistant imaging points from the transducer array center.

A 10.5 mm virtual source distance yields an adequate insonification and uniform SNR distribution in 90° imaging sector.

B. Noise in DWI

We performed the noise measurements using the method described in Sec. II E 1. Figure 5 shows the noise contribution for the total noise in DWI [for CGS(A) and CGS(B)] and one transmission in CSFI. The noise level in CSFI is discussed in Sec. VI.

We calculated the noise contribution in coded DWI using the respective reference signals, which are 8-chip coded signals with 0.5, 1, 1.5, and 2-cycles/chip. The unit of the received noise amplitude is dB//LSB. The noise contribution to the signal remains at the same level for all chip lengths since all reference signals in DWI are normalized to have the same energy, 8 LSB^2-s. Therefore, the correlator gain is the same for all reference signals.

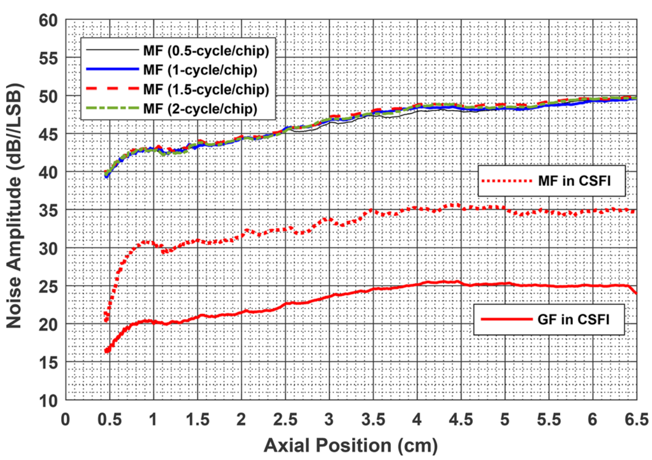

FIG. 5. (Color online) Noise measurement results for coded DWI (8 chips and $r_v = 10.5$ mm) with 4 different chip lengths. The noise amplitude variation with respect to depth is same for all chip lengths. This graph also shows the noise level in CSFI-GF and CSFI-MF. Note that the noise analysis for coded DWI (implemented with MF), CSFI-GF, and CSFI-MF have different gains. The average noise power is measured over independently taken 13 measurements without any transmission. The received noise amplitude is plotted in dB//LSB.

C. SNR along the arcs in speckle region

We measured the SNR of 8-bit coded DWI with 1-cycle/chip in the speckle region along the arcs positioned at different ranges. Figure 6 shows the SNR level and variation along the arcs at 20, 25, 40, and 50 mm ranges for 10.5 mm virtual source distance. The mean values of the SNR where the measurement variance is relatively high are also shown with a dotted line in Fig. 6. We estimated the imaging sector coverage based on the angle at which SNR drops by 3 dB from the mean value.

The imaging sectors are 95° and 90° for the arcs at 20 and 25 mm ranges, when r_v is 10.5 mm. At 20 mm range distance, a portion of the transmitted energy is wasted due to the five degrees of excess in the imaging sector. Therefore, it is possible to use a larger r_v to insonify the imaging sector at this range adequately. In the deeper regions, e.g., 40 and 50 mm ranges, the imaging sectors are 83° and 81°, respectively. In this case, using a smaller r_v would extend the imaging sector at these regions and provides 90° for the imaging sector. The imaging sector has approximately 88° (~90°) −6 dB beam width for both 40 and 50 mm ranges, and it is larger than 90° at closer ranges. Similar beam width is also obtained when other chip lengths are used in 8-bit coded transmission.

The geometrical divergence sector prediction for 10.5 mm virtual source distance and a 12.8 mm array size (64λ at 7.5 MHz) is $\varphi = 62.7°$ and not 90°. We achieved approximately 90° imaging sector at all ranges when r_v is 10.5 mm. The difference between the geometrical prediction and the actual (achieved) coverage is due to diffraction. If only geometrical considerations were used, the required source distance would be 6.4 mm. A source distance of 6.4 mm spreads the ultrasonic energy outside the region of interest and causes significant loss in SNR. Confining the insonification to the region of interest improves the SNR significantly.

Adequate insonification of the imaging sector must be considered in conjunction with the penetration depth since there is a trade-off between the SNR level and insonification

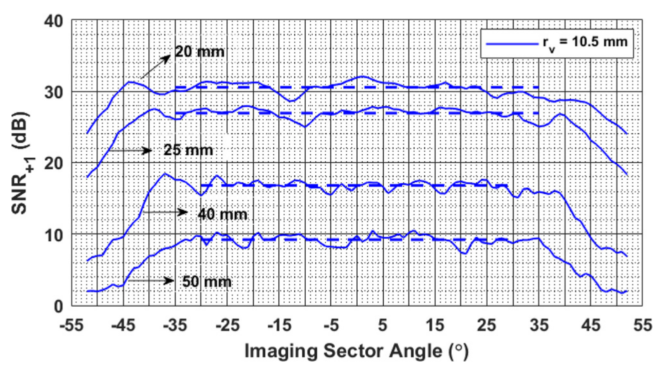

FIG. 6. (Color online) SNR of 8-bit coded DWI with 1-cycle/chip along the arcs at 20, 25, 40, and 50 mm ranges when r_v is 10.5 mm. The arcs constitute equidistant imaging points at which the attenuation remains same. The mean SNR values are also plotted with dashed lines where the measurement variance is relatively high.

angle. For example, if a single chip signal were used instead of an 8-bit coded signal, the penetration depth would be much lower, and a long r_v would yield the required beam width.

V. EFFECT OF CHIP SIGNAL LENGTH ON SNR

A. SNR in speckle

We investigated the effect of chip signal length on SNR for coded DWI. We measured SNR in the speckle region of the phantom.

Figure 7 shows the SNR_{+1} as a function of depth, obtained for coded DWI for four different chip signal lengths when r_v is 10.5 mm. An SNR level of 6 dB is marked to compare the penetration depth of different signals. The penetration depths obtained with 0.5, 1, 1.5, and 2 cycle/chip signals are 5.3, 5.6, 5.3, and 4.8 cm, respectively. The maximum penetration depth is obtained with 1 cycle/chip signal.

The SNR_{+1} obtained by coded DWI with longer chips is higher at closer depths. For example, SNR_{+1} of 2-cycles/chip signal is 2, 4.4, and 11.1 dB higher at 1 cm depth compared to SNR_{+1} of signals with 1.5, 1, and 0.5 cycle/chip lengths, respectively. This result conforms with the expectation that the correlator output will increase if the signal energy is increased.

SNR_{+1} difference decreases as the DW propagates and the order among 1, 1.5, and 2 cycle/chip lengths become reversed at about 2.5 cm depth. The coded signal with a 1-cycle/chip has the highest SNR_{+1} beyond 2.5 cm depth. The penetration depth is 8 mm larger than that of the 2-cycle/chip.

This result is counter-intuitive since a coded signal with 1-cycle/chip length has lower transmitted energy than 1.5

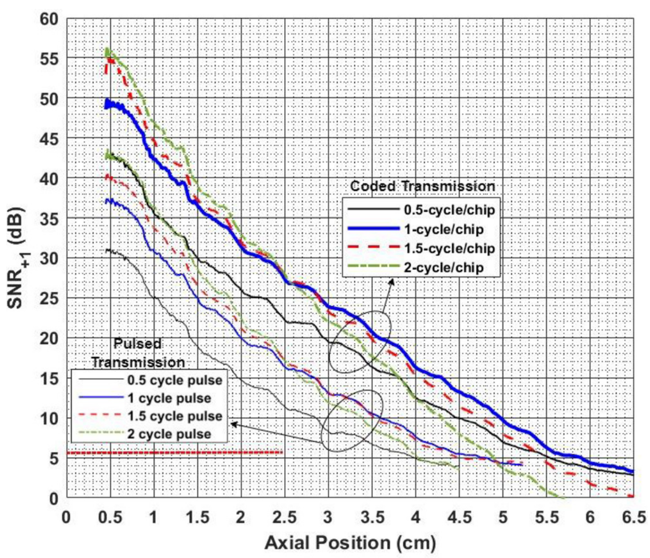

FIG. 7. (Color online) SNR_{+1} measurement results in speckle region for coded DWI (8 chips and $r_v = 10.5$ mm) with 4 different chip lengths and for pulsed DW transmission (1 chip and $r_v = 10.5$ mm) with 4 different pulse lengths. The ellipses show the pulsed and coded transmission curve families. Speckle amplitude is measured over 11 different measurements each yielding statistically independent data. 6-dB reference is also plotted with dotted line for penetration depth analysis.

and 2 cycle/chip signals. More transmitted energy leads to SNR improvement if the transmitted signals are coherently superimposed in the field. However, the coherent addition is not possible in general unless the signals are focused to a particular region by proper phasing. On the other hand, DWI inherently avoids the coherent addition of the transmitted signals in the field, which is more aggravated as the propagation distance increases. The signals with longer chip duration suffer more and undergo the destructive addition of chip signals. Furthermore, the signals scattered in the media interfere each other at every point in the field. Combined with propagation in multiple scattering medium, the diverging wave effect favors shorter chip signals for better SNR.

The shortest chip duration in this study also has a remarkable performance, as shown in Fig. 7. The penetration depth obtained by 0.5 cycle/chip signal is 5.3 cm, which is higher than the penetration depth of 2 cycle/chip signal. This signal is the shortest duration signal and has the lowest transmitted pressure amplitude. The SNR difference between this signal and the 1-cycle/chip signal is 6.6 dB at 0.5 cm depth, whereas it is 2.7 dB at 5 cm. Indeed, the received signal amplitude of the 0.5-cycle/chip signal in water is approximately half of the 1-cycle/chip signal (peak power is also 6 dB lower) because the 67% bandwidth of the transducer transfer function affects the 0.5-cycle signal more.[50] If the driving transmitted energy were the same for 0.5 and 1 cycle/chip signals energy, the peak amplitude would be approximately 100 V instead of 70 V for 0.5 cycle/chip signal. This equalization would result in a 3 dB increase in SNR and make 0.5 cycle/chip signal best in penetration depth.

Figure 7 also shows the SNR_{+1} for pulsed (uncoded) DWI with four different pulse lengths when r_v is 10.5 mm. The same dependence of SNR_{+1} to the chip length also exists in uncoded transmission, except the SNR levels are 12 dB lower. A difference of 3 dB is due to single transmission in uncoded case and 9 dB for 8-bit coding (see Sec. V C). Therefore, it is conjectured that SNR in any linear coding scheme will have a similar dependence on the chip length.

We show that the 67% two-way transducer bandwidth limits the maximum amplitude, and hence, the received signal's peak power.[50] The received 1-cycle signal has a maximum amplitude, which is only 80% of 2-cycle and 1.5-cycle signals. The latter two have the same maximum amplitude since there is sufficient time for the transient to develop. The 0.5-cycle signal suffers the most and remains at 40%. The 0.5-cycle received signal has approximately nine times less energy than the 2-cycle pulse, whereas the ratio of the energies of the respective drive signals is approximately 4-to-1.

B. SNR for pin targets

We also measured the SNR_{+1} at pin targets. Figure 8(a) shows the SNR_{+1} along the horizontal pin targets positioned at 40 mm depth. We achieved the maximum SNR_{+1} at the central pin target for all chip signal lengths. The SNR_{+1} of the coded signal with 1-cycle/chip is higher than that of the

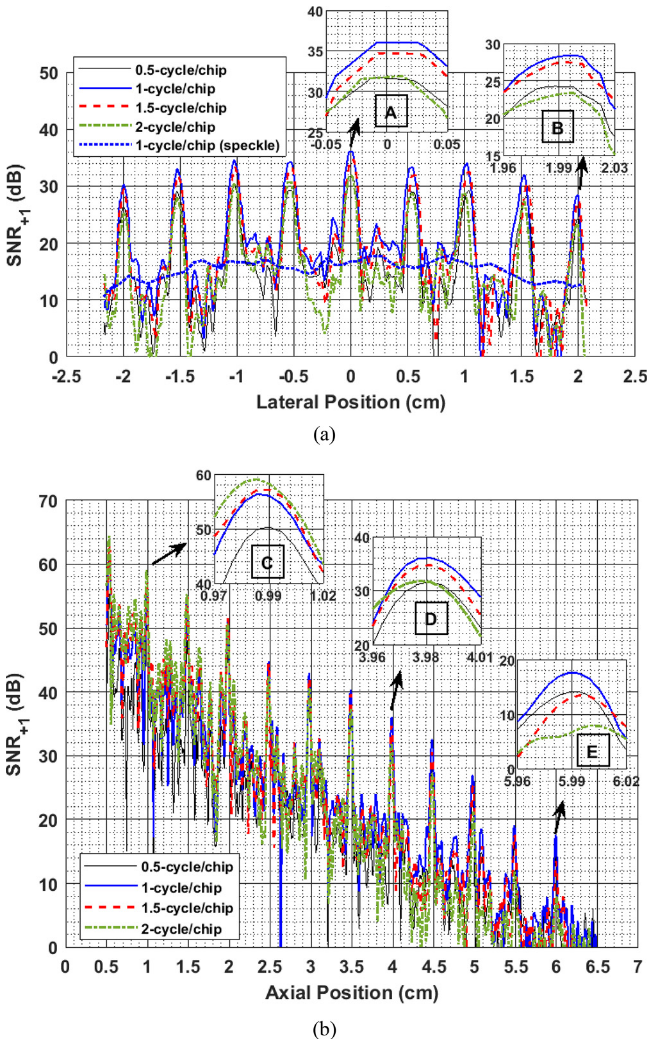

FIG. 8. (Color online) The SNR_{+1} for coded DWI (8 chips and $r_v = 10.5\,\text{mm}$) with 4 different chip lengths. (a) SNR_{+1} along the line of horizontal pin targets positioned at 40 mm depth. The SNR_{+1} along the horizontal direction in speckle region is also plotted on the same graph to make a comparison for speckle level variation. (b) SNR_{+1} along the line of vertical pin targets.

other coded signals in all horizontal pin targets. For example, it is 4.1 dB higher than that of the coded 2-cycle/chip signal at the central pin target (see inset A). The SNR_{+1} decreases along the line of horizontal pin targets away from the center for all chip lengths. This decrease is due to the effect of the attenuation on the increased path length at the outermost pin targets. Nevertheless, the SNR_{+1} of the coded signal with 1-cycle/chip is 5 dB higher than that of the coded signal with 2-cycle/chip (see inset B).

The speckle level variation between two pin targets is large and not smooth in Fig. 8(a). This is because the data had to be taken in a single transducer position in the pin target region. The SNR along the horizontal direction at 40 mm depth measured in the speckle region is also plotted in Fig. 8(a) for comparison.

Figure 8(b) depicts the SNR_{+1} variation along the line of vertical pin targets for all chip signal lengths. The variation is similar to the case in the speckle region. At closer depths, SNR is higher when chip length is longer (see inset C). For depths larger than 2.5 cm, again, the coded signal with 1-cycle/chip offers the maximum SNR (see insets D and E). The results shown in Fig. 8 are in agreement with those given in Fig. 7.

C. Effect of the code length on SNR

We also studied the performance of DWI with different code lengths.[55] We varied the code length from 2-to-10 bits and measured the SNR for a fixed chip signal length.

Theoretically, the SNR gain achieved by matched filtering is expressed as the time-bandwidth product of the signal. The time-bandwidth product of an uncoded signal is on the order of unity.[31] However, the coded signals have larger time bandwidth products,[31] which are equal to code sequence length, N. Therefore, the SNR gain in dB for a code length of N is $10 \times \log_{10}(N)$, if the coded signal is perfectly compressed with a matched filter.[24,28] We observed that the SNR improves when we increase the code length while the chip signal length is fixed. SNR increases by 3 dB for every doubling of the code length.

The SNR gain in 2-chip CGS coded signal compared to pulsed excitation (1-chip) is $10 \times \log_{10}(2N)$.[28] We measured that the SNR improves by 6 dB in 2-chip CGS coded signal compared to pulse transmission. The additional 3 dB in SNR gain is due to the two transmissions in 2-chip coded signal.

The SNR gain achieved from the measured data is in good agreement with the theoretical analysis.

VI. COMPARISON WITH FOCUSED IMAGING

We compared the SNR for DWI and CSFI on a single frame basis. Two different image features, the speckle and the pin targets, are used for comparison.

A. Noise in CSFI

The noise contribution per transmission is lowest in CSFI-GF as shown in Fig. 5. The noise amplitude is approximately 10 dB larger at every depth when MF is employed in CSFI. We calculated the noise contribution in CSFI-MF using 1-cycle pulse reference signal. Since there is an 8-to-1 energy difference between the reference signals of the CSFI-MF and DWI, the correlator provides a 9 dB gain to any signal detected using an 8-bit coded reference signal. There are two transmissions in the coded DWI, which adds another 3 dB to the noise level. In Fig. 5, the 12 dB noise level difference between DWI and CSFI-MF is clearly observable. Since the gains are different in each transmission scheme, the noise contributions in the received signals are also different. Therefore, the noise analysis for each scheme is required to obtain an accurate SNR measurement.

B. SNR comparison in the speckle region

The SNR_{+1} of the 8-chip coded DWI with 1-cycle/chip is compared to CSFI-GF and CSFI-MF in the speckle region

https://doi.org/10.1121/10.0009410

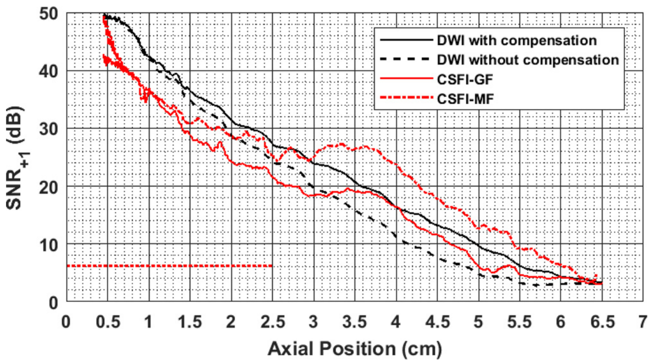

FIG. 9. (Color online) Speckle region SNR_{+1} measurement results for CSFI-GF, CSFI-MF and coded DWI (8 chips and $r_v = 10.5\,\text{mm}$). The maximum SNR is available in the vicinity of the focal region when CSFI-MF is used. In the nonfocal region, the coded DWI offers the highest SNR when attenuation compensation is applied. Note that the coded DWI with compensation offers higher SNR than the uncompensated case, while the results are similar at closer range. A 6-dB reference is plotted with a dotted line for penetration depth analysis.

in Fig. 9. To assess the compensation effect on SNR_{+1}, Fig. 9 also shows the SNR_{+1} of the coded DWI when the uncompensated two-way transmitted-and-received signal is used as the reference signal in MF. The SNR_{+1} of the coded DWI is 6.5 dB higher than the CSFI-GF up to 3 cm depth. SNR obtained by CSFI-GF is inferior to the coded DWI at all depths even in the focal region. The SNR values of the coded DWI and CSFI-GF are the same only at the focal depth (4 cm).

Coded DWI also offers better SNR compared to CSFI-MF up to 3 cm depth. However, the SNR of the latter scheme increases at the focal region and exceeds the SNR of coded DWI, reaching a maximum difference of 7.1 dB. Using MF with CSFI increases the effect of focusing gain, producing the highest SNR in the focal region.

It is clear from Fig. 9 that the compensation of the reference signal improves the SNR_{+1} of the coded DWI as the depth increases. At lower depths (e.g., 1 cm), compensation gives the same SNR_{+1} as the uncompensated case because the coded ultrasound beam does not alter significantly due to the attenuation. The effect of compensation becomes very significant at larger depths. For example, the SNR_{+1} of the compensated case is 5 dB larger at a depth of 4 cm. The penetration depth improves by approximately 7 mm (15%).

Figure 9 also shows the 6 dB reference for penetration depth. The 8-chip CGS-coded DWI offers a larger penetration depth (5.6 cm) than CSFI-GF. The penetration depth of the CSFI-GF is 5 cm, which is very close to the focus point. The penetration depth of the CSFI-MF (6 cm) is 4 mm larger than that of the coded DWI.

C. SNR comparison in the pin target region

The SNR variation along the horizontal pin targets positioned at 40 mm depth is shown in Fig. 10(a). The SNRs of the 8-chip coded DWI and CSFI-GF are similar (see inset F). If MF is used instead of GF in CSFI, the SNR improves by 6–8 dB and exceeds the SNR attained by coded DWI. The SNR of coded DWI is 6.5 dB less at the center pin (see inset F).

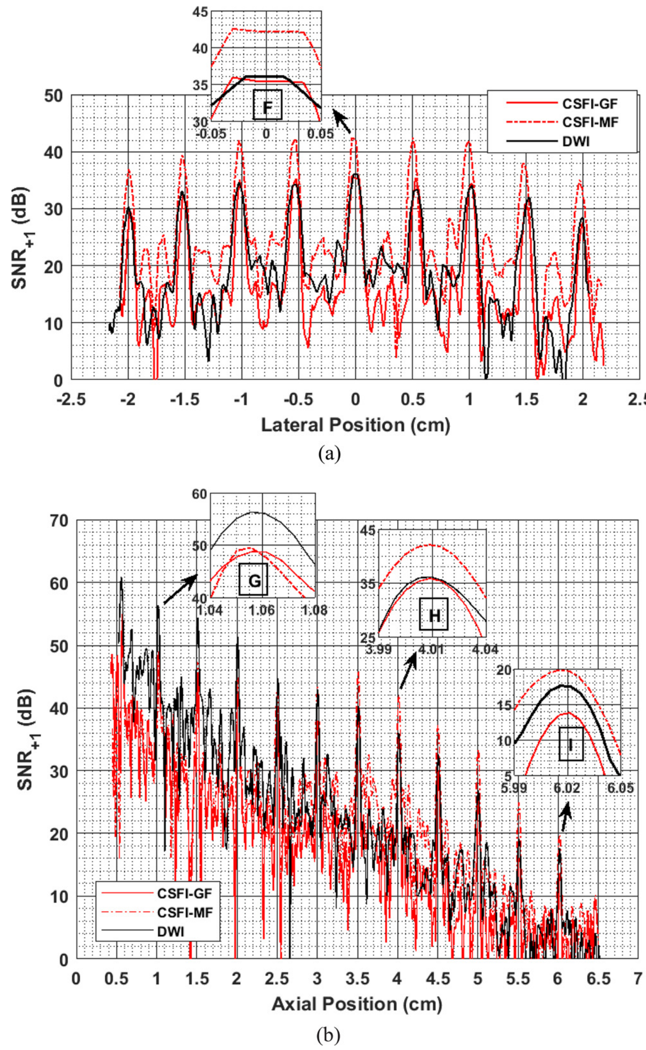

FIG. 10. (Color online) SNR for CSFI and coded DWI (8 chips and $r_v = 10.5\,\text{mm}$). CSFI-GF and CSFI-MF are shown for comparison. (a) SNR for horizontal pin targets at 40 mm depth (b) SNR for vertical pin targets.

Figure 10(b) clearly shows that the coded DWI has a significant SNR advantage over the CSFI-GF in the nonfocal region. For example, it is 7.6 dB larger at 1 cm depth (see inset G) and 3.8 dB larger at 6 cm depth (see inset I) compared to CSFI-GF. Coded DWI does not lose its SNR advantage even in the focal region. In the focal region, the CSFI-MF offers 6 dB better SNR than coded DWI (see inset H). However, the SNR of coded DWI is superior in the nonfocal regions. For example, it exceeds CSFI-MF by 7 dB at 1 cm depth.

D. SSR in DWI and CSFI

SSR is the ratio between the signal amplitude and the speckle amplitude in a pin target region. It reduces the perceived resolution of the pin target.[56]

We measured the SSR along the vertical line of pin targets. We calculated SSR as the difference between the signal amplitude at the pin targets and the speckle amplitude. Figure 11 shows the SSR in DWI, CSFI-GF, and CSFI-MF.

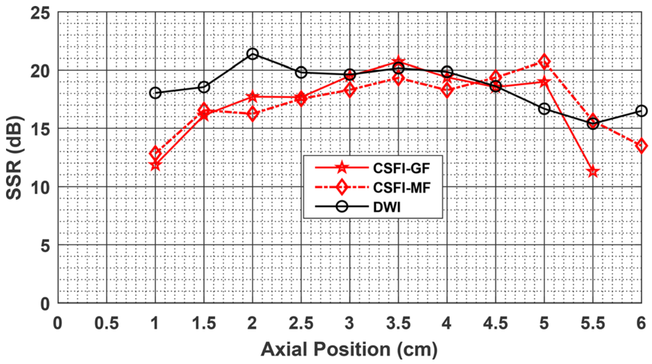

FIG. 11. (Color online) SSR of CSFI-GF, CSFI-MF, and coded DWI (8 chips, 1-cycle/chip, and $r_v = 10.5$ mm) along the vertical line of pin targets.

SSR in DWI maintains a level of 19 dB between 1.5 cm and 4.5 cm depths. SSR of CSFI is similar to that of the DWI with minor differences.

The pin targets in the phantom are relatively small and made of monofilament nylon. The pin target radius, a, is 1/8 of the wavelength at the center frequency, 7.5 MHz. The ka is 0.785, where k is the wavenumber. The average ka is even lower for the acoustic pulse in the medium since the acoustic signal energy is dominated by a lower frequency band as the attenuation becomes effective.[50] The nylon pin targets' reflection coefficient leads to a reflected signal amplitude which is 10 dB less than that of steel wire targets.[57] Hence, these pin targets are particularly suitable for SNR and SSR assessment.

VII. DISCUSSION OF RESULTS

A. Performance variation

DW transmission inherently avoids the coherent addition of the transmitted signals while the energy propagates in the medium. Coded signals, however, perform best when the signals are coherently summed up for maximum energy. This contradiction in combining the physics of DWs and the mathematics underlying coded signals manifests itself as maximum SNR is obtained in DWI when the chip signal is as short duration (wideband) as possible.

Short-duration signals have comparatively more energy at lower frequencies,[50] which also emerges as an advantage in a multiscattering environment where the attenuation is significant. As the depth increases, energy at lower frequencies prevail, and attenuation compensation is more effective in short-duration signals.

Coded DWI offers approximately 90° imaging sector when virtual source distance, r_v, is 10.5 mm. For this optimum virtual source distance, we compared the SNR performance with respect to the chip duration when the drive voltage amplitude is kept constant. Therefore, the energy of the shorter chip signals is lower. The signal with the shortest duration chip that the transducer can deliver to the medium with adequate peak power provides maximum SNR in DWI despite its lower energy. We used an array with a 67% two-way bandwidth in this work; signals with 1-cycle/chip yield the maximum SNR in coded DWI.

The minimum chip length can be 0.5-cycle, in which case the received signal suffers from the energy due to the two-way transducer transfer function. Despite this energy loss, the coded signal with 0.5 cycle/chip has excellent performance as far as SNR is considered. Consequently, the wider the transducer bandwidth, the higher the SNR.

The temporal resolution is 55.25 frames per second (fps) in CSFI when the image frame is constructed using 181 transmissions. However, we acquired one frame of CGS coded DW data in 200 μs in this study, which corresponds to 5000 fps. 8-chip coded DWI with 1-cycle/chip provides an approximately 90-fold increase in frame rate without compromising from SNR compared to CSFI even in the focal region.

We employed CGS as a code sequence in this study because these codes do not have any code range lobes. However, they require two transmissions, and the correlation properties of CGS-coded signals deteriorate in attenuating medium. In this respect, we expect that similar performance improvement is possible when other code sequences are employed. This issue must be investigated for possible improvements.

B. Limitations and potential improvements

The performance of coded transmission relies on maintaining a high correlation between the received coded signals and the reference signal. The similarity between the received signal and the reference signal determines the correlator output. The attenuation compensation increases this similarity, which yields an increase at the correlator output. We found out that using an attenuation compensated reference signal significantly improves the SNR. Refinement in the attenuation compensation of the reference signal will further improve the SNR. The effects of multi-layered medium with different attenuation conditions on code range lobes must also be investigated.

We did not use apodization in this work. Determination and use of appropriate apodization for DWI using optimized pulse length is a potential area for improvement.

The dataset used in this paper is available in a GitHub repository.[58]

C. Coded images

We presented the ultrasound images of the anechoic cyst targets for CSFI-GF, coded DWI with 1-cycle/chip and 2-cycle/chip in Figs. 12(a), 12(b), and 12(c), respectively. The anechoic cyst targets are encircled with a dotted line in Fig. 2. Each image is normalized with respect to its own maximum.[59] The dynamic range of the displayed images is 45 dB. We complemented the 2.3 dB/cm variable gain to 7.5 dB/cm in post-processing before constructing the images (see Sec. II E 1). Note that 7.5 dB/cm compensates for the two-way attenuation calculated at the center frequency.

The SNR performances of different imaging settings can be comparatively evaluated at the regions of low SNR, where the signal power is low and noise becomes significant. The image quality is inevitably low in such regions

https://doi.org/10.1121/10.0009410

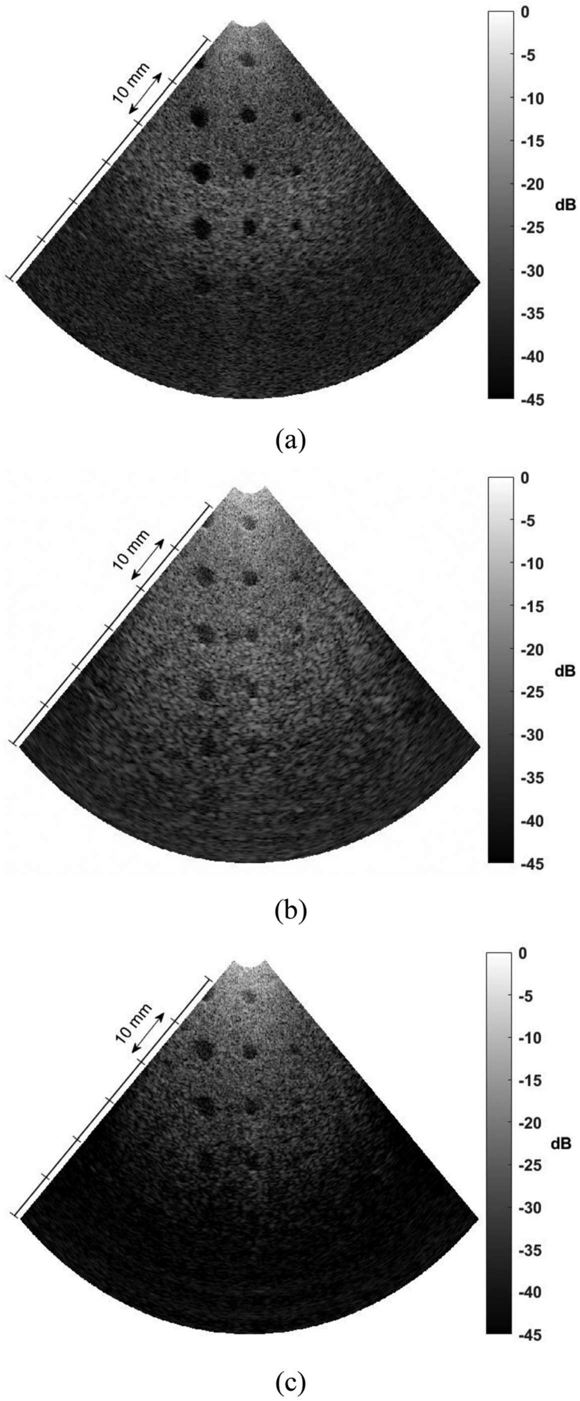

FIG. 12. Ultrasound images of the anechoic cyst targets. A dynamic range of normalized image intensity values are from 0 to −45 dB. (a) CSFI-GF image constructed by 181 focused transmissions. (b) 1-cycle/chip coded DWI image. (c) 2-cycle/chip coded DWI image. Coded DWI images are constructed by using two transmissions (acquired in 200 μs) and attenuation compensation.

and main problem becomes to detect the presence of various features. The vicinity of the penetration depth is such a region. The anechoic cyst targets are particularly suitable for assessing the SNR and noise-related imaging performance. The signal level in the cyst region is similar to the noise level at low SNR regions, whereas the speckle signal level in the nearby region depends on the depth.

The CSFI-GF image is shown in Fig. 12(a) as a reference. The focusing gain in the vicinity of the transmit focus at 40 mm depth manifests itself as an increased brightness in the image. The anechoic cysts at 50 mm depth are barely visible since the penetration depth of the CSFI-GF is 50 mm, as shown in Fig. 9. On the other hand, the anechoic cyst targets at 60 mm depth are not visible.

DWI with 1-cycle/chip is shown in Fig. 12(b), where the SNR and the penetration depth improvement can be observed. All the anechoic cyst targets up to 50 mm depth are visible, but those at 60 mm depth are barely visible. This result complies with the penetration depth of the coded DWI with 1-cycle/chip, which is 56 mm, as shown in Fig. 9. Note that the comparison between CSFI-GF and coded DWI is performed on a single frame basis. There are almost 90 times fewer transmission events in DWI compared to CSFI-GF.

When the chip signal duration is increased from 1-cycle to 2-cycle in coded transmission, the penetration depth decreases to 48 mm, as shown in Fig. 7. This decrease is visible in Fig. 12(c) since the anechoic cyst targets at 50 mm depth are not visible. It is also shown in Fig. 7 that the SNR decreases rapidly down to 0 dB after the penetration depth when coded signal with 2-cycle/chip is transmitted. This decrease appears as the darker region in Fig.12(c).

The clarity and definition in all images are in agreement with the quantitative analysis results.

ACKNOWLEDGMENTS

This work was supported by the Scientific and Technological Research Council of Turkey (TUBITAK) under Grant No. 119E509.

[1]L. Demi, "Practical guide to ultrasound beamforming: Beam pattern and image reconstruction analysis," Appl. Sci. **8**(9), 1544 (2018).

[2]E. Badescu, D. Garcia, P. Joos, A. Bernard, L. Augeul, R. Ferrera, M. Viallon, L. Petrusca, D. Friboulet, and H. Liebgott, "Comparison between multiline transmission and diverging wave imaging: Assessment of image quality and motion estimation accuracy," IEEE Trans. Ultrason. Ferroelectr. Freq. Control. **66**, 1560–1572 (2019).

[3]N. Bottenus, "Comparison of virtual source synthetic aperture beamforming with an element-based model," J. Acoust. Soc. Am. **143**, 2801–2812 (2018).

[4]K. Kaburaki, M. Mozumi, and H. Hasegawa, "Estimation of two-dimensional motion velocity using ultrasonic signals beamformed in cartesian coordinate for measurement of cardiac dynamics," Jpn. J. Appl. Phys. **57**, 07LF03 (2018).

[5]E. Roux, F. Varray, L. Petrusca, C. Cachard, P. Tortoli, and H. Liebgott, "Experimental 3-D ultrasound imaging with 2-D sparse arrays using focused and diverging waves," Sci. Rep. **8**, 9108 (2018).

[6]M. Correia, J. Provost, S. Chatelin, O. Villemain, M. Tanter, and M. Pernot, "Ultrafast harmonic coherent compound (UHCC) imaging for high frame rate echocardiography and shear-wave elastography," IEEE Trans. Ultrason. Ferroelectr. Freq. Control **63**, 420–431 (2016).

[7]C. Samson, R. Adamson, and J. A. Brown, "Ultrafast phased-array imaging using sparse orthogonal diverging waves," IEEE Trans. Ultrason. Ferroelectr. Freq. Control. **67**, 2033–2045 (2020).

[8]J. Kang, D. Go, I. Song, and Y. Yoo, "Wide field-of-view ultrafast curved array imaging using diverging waves," IEEE Trans. Biomed. Eng. **67**, 1638–1649 (2020).

[9]D. Posada, J. Porée, A. Pellissier, B. Chayer, F. Tournoux, G. Cloutier, and D. Garcia, "Staggered multiple-PRF ultrafast color Doppler," IEEE Trans. Med. Imag. **35**, 1510–1521 (2016).

[10]D. T. Blackstock, *Fundamentals of Physical Acoustics* (Wiley, New York, 2000), pp. 472–488.

[11]D. J. Shull, E. E. Kim, M. F. Hamilton, and E. A. Zabolotskaya, "Diffraction effects in nonlinear Rayleigh wave beams," J. Acoust. Soc. Am. **97**, 2126–2137 (1995).
[12]A. Aubry and A. Derode, "Multiple scattering of ultrasound in weakly inhomogeneous media: Application to human soft tissues," J. Acoust. Soc. Am. **129**, 225–233 (2011).
[13]J. A. Jensen, "Medical ultrasound imaging," Prog. Biophys. Mol. Biol. **93**, 153–165 (2007).
[14]Z. He, F. Zheng, Y. Ma, H. H. Kim, Q. Zhou, and K. K. Shung, "A sidelobe suppressing near-field beamforming approach for ultrasound array imaging," J. Acoust. Soc. Am. **137**, 2785–2790 (2015).
[15]C. Papadacci, M. Pernot, M. Couade, M. Fink, and M. Tanter, "High-contrast ultrafast imaging of the heart," IEEE Trans. Ultrason. Ferroelectr. Freq. Control. **61**, 288–301 (2014).
[16]H. Hasegawa and H. Kanai, "High-frame-rate echocardiography using diverging transmit beams and parallel receive beamforming," J. Med. Ultrason. **38**, 129–140 (2011).
[17]J. Grondin, V. Sayseng, and E. E. Konofagou, "Cardiac strain imaging with coherent compounding of diverging waves," IEEE Trans. Ultrason. Ferroelectr. Freq. Control. **64**, 1212–1222 (2017).
[18]J. Porée, D. Posada, A. Hodzic, F. Tournoux, G. Cloutier, and D. Garcia, "High-frame-rate echocardiography using coherent compounding with Doppler-based motion-compensation," IEEE Trans. Med. Imag. **35**, 1647–1657 (2016).
[19]Y. Takeuchi, "An investigation of a spread energy method for medical ultrasound systems: Part one: Theory and investigation," Ultrasonics **17**, 175–182 (1979).
[20]M. O'Donnell, "Coded excitation system for improving the penetration of real-time phased-array imaging systems," IEEE Trans. Ultrason. Ferroelectr., Freq. Control. **39**, 341–351 (1992).
[21]K. L. Gammelmark and J. A. Jensen, "Multielement synthetic transmit aperture imaging using temporal encoding," IEEE Trans. Med. Imag. **22**, 552–563 (2003).
[22]S. Nikolov and J. A. Jensen, "Comparison between different encoding schemes for synthetic aperture imaging," in *Medical Imaging 2002: Ultrasonic Imaging and Signal Processing* (SPIE, Bellingham, WA, 2002), Vol. 4687, pp. 1–12.
[23]A. Lahav, T. Chernyakova, and Y. C. Eldar, "FoCUS: Fourier-based coded ultrasound," IEEE Trans. Ultrason. Ferroelectr. Freq. Control. **64**, 1828–1839 (2017).
[24]J. Zhao, Y. Wang, J. Yu, T. Li, and Y. P. Zheng, "Feasibility of coded vibration in a vibro-ultrasound system for tissue elasticity measurement," J. Acoust. Soc. Am. **140**, 35–44 (2016).
[25]R. Kažys, L. Svilainis, and L. Mažeika, "Application of orthogonal ultrasonic signals and binaural processing for imaging of the environment," Ultrasonics **38**, 171–175 (2000).
[26]J. Shen and E. S. Ebbini, "A new coded-excitation ultrasound imaging system. I. Basic principles," IEEE Trans. Ultrason. Ferroelectr. Freq. Control. **43**, 131–140 (1996).
[27]I. Trots, A. Nowicki, W. Secomski, and J. Litniewski, "Golay sequences–side lobe–cancelling codes for ultrasonography," Archives Acoust. **29**, 87–97 (2004).
[28]X. Wang, J. Yang, J. Ji, Y. Zhang, and S. Zhou, "Research on Golay-coded excitation in real-time imaging of high frequency ultrasound biomicroscopy," Nature **11**, 1–12 (2021).
[29]R. Y. Chiao and X. Hao, "Coded excitation for diagnostic ultrasound: A system developer's perspective," IEEE Trans. Ultrason. Ferroelectr. Freq. Control. **52**, 160–170 (2005).
[30]C. Leavens, R. Willams, P. Burns, and M. Sherar, "The use of phase codes in ultrasound imaging: SNR gain and bandwidth requirements," Appl. Acoust. **70**, 1340–1351 (2009).
[31]T. Misaridis and J. A. Jensen, "Use of modulated excitation signals in medical ultrasound. Part I: Basic concepts and expected benefits," IEEE Trans. Ultrason. Ferroelectr. Freq. Control. **52**, 177–191 (2005).
[32]T. Misaridis and J. A. Jensen, "Use of modulated excitation signals in medical ultrasound. Part II: Design and performance for medical imaging applications," IEEE Trans. Ultrason. Ferroelectr. Freq. Control. **52**, 192–207 (2005).
[33]T. Misaridis and J. A. Jensen, "Use of modulated excitation signals in medical ultrasound. Part III: High frame rate imaging," IEEE Trans. Ultrason. Ferroelectr. Freq. Control. **52**, 208–219 (2005).
[34]B. Lashkari, A. Manbachi, A. Mandelis, and R. S. C. Cobbold, "Slow and fast ultrasonic wave detection improvement in human trabecular bones using Golay code modulation," J. Acoust. Soc. Am. **132**, 222–228 (2012).
[35]F. Zhao, L. Tong, Q. He, and J. Luo, "Coded excitation for diverging wave cardiac imaging: A feasibility study," Phys. Med. Biol. **62**, 1565–1584 (2017).
[36]I. Trots, "Mutually orthogonal Golay complementary sequences in synthetic aperture imaging systems," Arch. Acoust. **40**, 283–289 (2015).
[37]F. Zhao and J. Luo, "Diverging wave compounding with spatio-temporal encoding using orthogonal Golay pairs for high frame rate imaging," Ultrasonics **89**, 155–165 (2018).
[38]L. J. Thomas and R. Y. Chiao, "Method and apparatus for ultrasonic synthetic transmit aperture imaging using orthogonal complementary codes," U.S. patent No. 6,048,315 (April 11, 2000).
[39]P. Gong, P. Song, and S. Chen, "Ultrafast synthetic transmit aperture imaging using Hadamard-encoded virtual sources with overlapping sub-apertures," IEEE Trans. Med. Imag. **36**, 1372–1381 (2017).
[40]P. Gong, M. C. Kolios, and Y. Xu, "Delay-encoded transmission and image reconstruction method in synthetic transmit aperture imaging," IEEE Trans. Ultrason. Ferroelectr. Freq. Control. **62**, 1745–1755 (2015).
[41]Y. Zhang, Y. Guo, and W. Lee, "Ultrafast ultrasound imaging with cascaded dual-polarity waves," IEEE Trans. Medical Imaging. **37**, 906–917 (2018).
[42]Y. Zhang, H. Li, and W.-N. Lee, "Imaging heart dynamics with ultrafast cascaded-wave ultrasound," IEEE Trans. Ultrason. Ferroelectr. Freq. Control. **66**, 1465–1479 (2019).
[43]T. Harrison, A. Sampaleanu, and R. J. Zemp, "S-sequence spatially encoded synthetic aperture ultrasound imaging Correspondence," IEEE Trans. Ultrason. Ferroelectr. Freq. Control. **61**, 886–890 (2014).
[44]A. Ramalli, F. Guidi, E. Boni, and P. Tortoli, "A real-time chirp-coded imaging system with tissue attenuation compensation," Ultrasonics **60**, 65–75 (2015).
[45]J. Kang, Y. Kim, W. Lee, and Y. Yoo, "A new dynamic complex baseband pulse compression method for chirp-coded excitation in medical ultrasound imaging," IEEE Trans. Ultrason. Ferroelectr. Freq. Control. **64**, 1698–1710 (2017).
[46]R. S. C. Cobbold, *Foundations of Biomedical Ultrasound* (Oxford University Press, New York, 2007), p. 530.
[47]U. Madhow, *Fundamentals of Digital Communication* (Cambridge University, New York, 2008), p. 55.
[48]D. Z. Dokovic, "Equivalence classes and representatives of Golay sequences," Discr. Math. **189**, 79–93 (1998).
[49]J. G. Proakis, *Digital Communications*, 4th ed. (McGraw-Hill, New York, 2001), p. 234.
[50]Y. Kumru and H. Köymen, "Ultrasonic array characterization in multiscattering and attenuating media using pin targets," arxiv:2105.14816 (2021).
[51]H. Liebgott, R. Prost, and D. Friboulet, "Pre-beamformed RF signal reconstruction in medical ultrasound using compressive sensing," Ultrasonics **53**, 525–533 (2013).
[52]B. Carlson, *Communication Systems: An Introduction to Signals and Noise in Electrical Communication* (McGraw-Hill, New York, 1968), p. 495.
[53]K. F. Üstüner and G. L. Holley, *Ultrasound Imaging System Performance Assessment* (Siemens Medical Solutions, Mountain View, CA, 2003).
[54]H. Eriksson, P. O. Borjesson, P. Odling, and N. Holmer, "A robust correlation receiver for distance estimation," IEEE Trans. Ultrason. Ferroelectr. Freq. Control. **41**, 596–603 (1994).
[55]Y. Kumru and H. Köymen, "Coded divergent waves for fast ultrasonic imaging: Optimization and comparative performance analysis," arXiv:2104.10526 (2021).
[56]D. Hyun, L. L. Brickson, K. T. Looby, and J. J. Dahl, "Beamforming and speckle reduction using neural networks," IEEE Trans. Ultrason. Ferroelectr. Freq. Control. **66**, 898–910 (2019).
[57]W. G. Neubauer, *Underwater Acoustic Reflection from Surfaces and Shapes* (Peninsula Publishing, Newport Beach, CA, 2017). pp. 225-233.
[58]Y. Kumru and H. Köymen, "Signal and noise data for divergent acoustic waves," GitHub, https://github.com/YasinKUMRU/Signal-and-Noise-Data-for-Divergent-Acoustic-Waves (2021) (Last viewed February 6, 2022).
[59]L. Demi, M. Demi, R. Prediletto, and G. Soldati, "Real-time multi-frequency ultrasound imaging for quantitative lung ultrasound-first clinical results," J. Acoust. Soc. Am. **148**, 998–1006 (2020).